

Material-Dependent Reaction Anisotropy in Two-Dimensional Transition Metal Dichalcogenides

Myeongin Song,¹ Haneul Kang,¹ Dan Rhodes,² Bumho Kim,² James Hone,² and Sunmin Ryu^{1*}

¹Department of Chemistry, Pohang University of Science and Technology (POSTECH), Pohang, Gyeongbuk 37673, Korea

²Department of Mechanical Engineering, Columbia University, New York, NY 10027, USA

* E-mail: sunryu@postech.ac.kr

Abstract

Anisotropic material properties of two-dimensional (2D) crystals are not only intriguing but also of potential use for many applications. In this work, we report the anisotropy of bond-breaking reactions is governed by the structural anisotropy and significantly material-dependent for 2D semiconducting transition metal dichalcogenides (TMDs). The degree of the anisotropy that led to trigonal oxidation patterns was much higher in MoS₂ and MoSe₂ than WS₂ and WSe₂. Using optical second-harmonic generation spectroscopy, we establish crystal-facet-resolved kinetic measurements and show that the reactions proceed fastest (slowest) for chalcogen (metal)-terminated zigzag edges. Edge-specific reaction rates fed into kinetic Wulff construction also verified the material-dependent anisotropy. We also show that the reactions are initiated at substrate-mediated defects that are located on the bottom and top surfaces of 2D TMDs.

KEYWORDS: anisotropic reactions, second-harmonic generation, two-dimensional crystals, transition metal dichalcogenides

Surfaces are an essential part of functional materials because they accommodate various physical and chemical exchanges in the form of energy and charges at the interface with other chemical entities. Heterogeneous catalysis enabling low-cost synthesis of various commercial chemicals¹ also relies on the chemical instability of exposed surfaces that form intermediate bonds during reactions. Because of their high surface-atom fraction, this statement is most relevant to two-dimensional (2D) materials represented by graphene and transition metal dichalcogenides (TMDs). Facile charge exchange with adsorbed molecules across the surface enabled controlling charge density of 2D materials through chemical doping of electrons and holes.²⁻⁷ Photogenerated excitonic energy is transferred from or to 2D materials via ultrafast dipolar quenching.⁸⁻¹¹ For many physicochemical processes, however, their atomically flat surfaces are much less active than their edges or point defects,^{2, 12, 13} which constitute their 1D and 0D surfaces, respectively. These sub-2D surfaces also support novel phenomena and modification of material properties such as vacancy-induced mid-gap states,¹⁴ edge-state-mediated magnetism,¹⁵ edge-enhanced photoluminescence¹⁶ and optical second-harmonic generation (SHG).¹⁷

For nanoscale control of edge structures, 2D crystals serve as a good testbed because of their sheet-like geometry that allows facile lithographic write-and-cut in addition to their high crystallinity and chemical stability. Besides the conventional lithographic methods for microfabrication, various chemical reactions have been explored for controlled patterning of graphene: thermal oxidation for circular patterns,² activated hydrogen plasma for zigzag-terminated hexagons,¹⁸ and dynamic control between zigzag and armchair edges.¹⁹ In this regard, the family of TMDs presents more possibilities of control as binary compounds. 2D MoS₂ was found to develop zigzag-terminated²⁰ triangular patterns upon thermal oxidation.²¹⁻²² Controlling the concentration of precursors also enabled selective growth

of MoS₂ with specific edges²³ in agreement with a stochastic model based on site-dependent activation energy.²⁴ Despite these studies, however, 2D TMDs await further sophisticated investigations for chemical manipulation of edges and defects, and understanding the underlying principles pertaining to 2D material systems. Most of all, the material dependence of given reactions has yet to be comprehended for custom-tailored patterning. Moreover, one needs to understand the reaction kinetics at edges that may vary as a function of their crystallographic orientation. Further insight is also required into the roles of atomic-level defects and interfaces with substrates in the initiation and propagation of the chemical reactions.

In this work, we report material-dependent anisotropy in the thermal oxidation of four 2D TMDs by establishing edge-resolved kinetic measurements based on optical second-harmonic generation (SHG) spectroscopy. W dichalcogenides exhibited rounded triangles of W oxides unlike Mo dichalcogenides showing equilateral triangular etch pits. The material-dependent anisotropy and branching between the oxide formation and etching are governed by the energy difference between competing edges and the thermal stability of oxides, respectively. The overall triangular shapes were supported by kinetic Wulff construction based on the experimental edge-specific rates but with noticeable deviation for W diselenides. We also show that the reactions are initiated at substrate-mediated defects that are located on the bottom and top surfaces of 2D TMDs. The reported methods and findings can be applied to other low-dimensional materials and will contribute toward elucidating underlying chemical principles and realizing customized control of edges.

Results and discussions

Varying anisotropy in oxidation of four TMDs. Single and few-layer TMD samples of four kinds (MX₂: M = Mo or W, X = S or Se) were prepared by mechanical exfoliation of commercial 2H-type bulk crystals (see Methods). The thickness and quality of the samples were characterized using Raman

spectroscopy, reflectance contrast, and atomic force microscopy (AFM) as described elsewhere.²⁰ Figures 1a ~ 1d show AFM images of four 1L TMDs obtained after oxidation at 280 ~ 380 °C. Whereas their reactions may be represented by the following generic equation, $2\text{MX}_2 + 7\text{O}_2 \rightarrow 2\text{MO}_3 + 4\text{XO}_2$,²¹⁻²² the four TMDs varied drastically in their reaction-induced nanoscopic patterns. As shown in the height images of MoS_2 and MoSe_2 (Figs. 1a & 1b), oxidation led to the triangular etch pits (TEs) that were almost equilateral and aligned in the same direction. The TE areas in MoX_2 were 1.1 ± 0.2 nm lower than unreacted areas and revealed bare substrates as shown in their phase images (Fig. S1). The triangular shapes found in the phase images of WS_2 and WSe_2 , however, were significantly rounded at their apexes (Figs. 1c & 1d). Remarkably, their height images revealed that the rounded triangles in WX_2 were protrusions slightly higher than unreacted regions (Figs. S1c & S1d). The substantial phase decrease³⁰ for the triangular areas indicated their chemical transformation. The optical bleaching and disappearance of Raman and photoluminescence peaks characteristic of WS_2 (Fig. S2) suggested that the triangles of WX_2 are tungsten oxides. Complete etching in MoX_2 indicates that most stoichiometric (MoO_3 , SO_2 , and SeO_2) and non-stoichiometric products are volatile at the reaction temperature, which is consistent with the fact that clusters of Mo oxides and suboxides sublime readily unlike bulk MoO_3 .³¹ Solidification as triangular oxides (TOs) observed for WX_2 is attributed to the higher thermal stability of W oxides (m.p. = 1473 °C) compared with Mo oxides (m.p. = 802 °C).³² It is also to be noted that the density of TEs and TOs is much higher for MSe_2 than MS_2 , which will be discussed later.

SHG-determined crystallographic orientations of triangles. Although less conspicuous because of their highly curved edges, TOs of WX_2 were also aligned in parallel. To determine the crystallographic orientation of the triangular patterns, we employed SHG spectroscopy, which detects the frequency-doubled signals of an incident fundamental beam. Because of their non-centrosymmetry and strong light-matter interaction, 1L of the four TMDs serve as efficient SHG media.³³ For angle-resolved SHG measurements, samples were rotated by an azimuthal angle (θ) with respect to the polarization direction of the fundamental beam (\vec{E}_ω), while the SH field ($\vec{E}_{2\omega}$) parallel to \vec{E}_ω was selected (Fig. 1e). The

symmetry of their second-order susceptibility tensor requires that the parallel SHG intensity (I_{SHG}) is proportional to $\cos^2 3\theta$ and reach maxima when \vec{E}_ω is parallel to the crystallographic armchair (AC) direction of the lattice.³³

Figure 1f shows the polar graph of I_{SHG} obtained from the oxidized WSe₂ sample. The data well fit with the predicted function indicated that one of the AC directions is at $\sim 16^\circ$ with respect to the horizontal axis of the polar graph. For the other TMDs, their AC directions were also determined with SHG measurements (Fig. S3) and designated with double-headed arrows in Fig. 1a ~ 1d. It can be readily seen that all the edges of TEs and TOs are parallel to zigzag (ZZ) directions that are normal to the AC lines. As depicted in Fig. 1e, two types of ZZ edges can be formed without considering lattice reconstruction: M-terminated (ZZ_M) and X-terminated (ZZ_X). As the controversy²¹⁻²² over the two possibilities was resolved by recent transmission electron microscopy studies,³⁴⁻³⁵ TEs and TOs found in this study were accordingly assigned to be ZZ_M-terminated.

Top and bottom surfaces subject to reactions. Unlike 1Ls, multilayered MoS₂ and MoSe₂ exhibited TOs instead of TEs (Figs. 2a & 2b). Whereas the TO in MoS₂ (Fig. 2a) spanned the 2L and 1L areas, the latter was completely etched away as shown in Fig. 1a. This indicates that TOs are formed by the oxidation of the bottommost layer contacting SiO₂ substrates. For TOs (Mo oxides including suboxides) to be formed in MoX₂ multilayers, oxygen molecules diffuse through the TMD-substrate interfaces and reach reaction centers at elevated temperatures.²⁰ One type of product in the form of Mo oxides and their oligomers³¹ does not diffuse efficiently because of their large size and remain within the triangle forming TOs. In contrast, chalcogen oxides (SO₂ or SeO₂) may diffuse out because of their small size. The TOs in MoX₂ are clearly visible in their phase images (Fig. S4), supporting that they are chemically distinct from the pristine areas. It is also notable that the vertices and edges of TEs are more rounded than those of TOs (Figs. 1a & 2a), which will be discussed below. Whereas TEs were also found in 2 ~ 4L MoS₂ and MoSe₂ as shown in Fig. S5, they were several times smaller than TOs. Unlike monolayer TEs (Fig. S1), the TEs of multilayer MoX₂ were not discernible in their phase images (Fig. S5), because

etch-pit regions also contain and expose pristine MoX_2 .

In multilayer WS_2 and WSe_2 , TOs were clearly visible in the phase images (Fig. 2c & 2d) and found to be slightly elevated (Fig. S4c & S4d) as in 1L. As will be discussed below, however, their shapes are more rounded than those in 1L WX_2 . Because W oxides formed in 1L WX_2 were found to survive the oxidation temperatures unlike Mo oxides, some of TOs may be located in the topmost layers of multilayer WX_2 . To distinguish the exposed TOs from hidden TOs, we performed lateral force microscopy (LFM) for oxidized 2L WSe_2 showing multiple TOs in its height image (Fig. 2e & 2f). As depicted in Fig. 2g, the tip in a contact AFM mode essentially measures the friction against the surface of samples during LFM scans.³⁶ Whereas some TOs in 2L WSe_2 were conspicuous in their LFM image (Fig. 2f), the others could hardly be discerned from the unreacted areas unlike their height image. Because the surfaces of intact TMDs exhibit extremely low friction compared to oxides including silica substrates,³⁶ the low-friction (high-friction) triangles were assigned to TO_B (TO_T) that were formed in the bottommost (topmost) layers. The effective frictional coefficient of TO_T including those in 1L was four times higher than that of TO_B (Fig. 2h). Notably, the average density was 10 times higher for TO_B than TO_T (Fig. 2e). This fact indicates that the reaction centers are more abundant in the bottommost layers, which will be justified below.

Quantification of anisotropy and kinetic Wulff construction. As depicted for 4L MoS_2 (Fig. 2a), we quantified the roundness of the triangular structures by the anisotropy index (R) defined as the ratio between the radii of the two circles that inscribes in and circumscribes on each triangle, respectively. R of 4L MoS_2 obtained from multiple TOs was 0.60 ± 0.03 , which is noticeably higher than 0.5 for an equilateral triangle. Notably, the anisotropy index was higher for 1L than multilayers of MoS_2 (Fig. 2i). On the other hand, rounded TOs of 4L WS_2 resulted in a higher anisotropy value of 0.92 ± 0.04 and decreased for thinner layers as shown in Fig. 2i. Remarkably, MoSe_2 and WSe_2 exhibited thickness-dependent R values that are similar to MoS_2 and WS_2 , respectively, which suggests that the anisotropic propagation of the reactions is mainly governed by the metallic elements of TMDs.

The material-dependent anisotropy observed in the oxidized 2D TMDs is dictated by the competition among different types of edges with varying oxidation rates. As depicted in Fig. 3a, the reaction centers of TEs or TOs at their early stage can be approximated as a tiny dodecagonal hole terminated with 6 armchair (AC) and 6 zigzag (ZZ) edges. One half (ZZ_M) of the latter exposes metallic atoms with the other half (ZZ_X) exposing chalcogens. We note, however, that the chemical structures given in Fig. 3a should be taken symbolically because multiple structures of similar formation energies are likely to exist for each of AC and ZZ edges.^{34-35, 37} Moreover, the edge structures of TEs and TOs can be affected by the oxidation that may induce reconstruction of edges.^{21, 35} According to the kinetic Wulff construction (KWC) theory,³⁷⁻³⁹ the edges with a higher rate (k) are consumed faster and become smaller in abundance. As the reaction proceeds further, the dodecagonal seed will grow and be terminated with the edges with the lowest k . Assuming that etch pits consist of the three types of edges, total 13 distinctive sets of (k_{ZZM} , k_{ZZX} , k_{AC}) that are different in the order of magnitude are possible as summarized in Fig. S6. The KWC theory predicts that each combination eventually leads to either of a triangle, hexagon, nonagon, or dodecagon as shown in Fig. 3b. It can be seen that the most anisotropic reactions generating triangles may result from multiple sets with either of k_{ZZM} or k_{ZZX} smallest. For the nondegenerate cases where the three rates are different from each other (cases 1 ~ 6 in Fig. S6), the starting dodecagon eventually turns into a triangle unless k_{AC} is smallest. For the degenerate cases (cases 7 ~ 13 in Fig. S6), triangular patterns can also be formed when either type of ZZ edges is slowest in the reaction rate. Although the anisotropy index values given in Fig. 2i do not pinpoint which case each TMD belongs to, it can be concluded that k_{ZZM} is smallest based on the aforementioned crystallographic assignment on edges of TEs and TOs. Moreover, the minimum/maximum ratio among the three rates is larger for WX_2 than MoX_2 because the anisotropy index of rounded triangles is determined by the ratio.

Edge-resolved determination of reaction rates. To corroborate the above model, we determined edge-specific oxidation rates of $MoSe_2$ and WSe_2 . As shown in Fig. 4a and 4b, oxidation left residues along the original edges of the pristine TMDs. The assignment could be confirmed by the linear residues

(marked by red arrows) that bisect the trench-like W oxide band (Fig. 4b). This fact also indicates that the 1L WSe₂ sample originally contained a crack line where the residues are located.⁴⁰ The oxidation rate of an edge was defined as the distance (d) between the two edges before and after the reaction divided by the duration of oxidation. For MoSe₂ and WSe₂, the degree of oxidation varied significantly depending on the direction of edges. In particular, ZZ_{Se} edges that were anti-parallel to ZZ_{Mo} of TEs in MoSe₂ underwent oxidative etching twice faster than ZZ_{Mo} (Fig. 4a).

For quantitative understanding, angle-specific oxidation rate (k_θ) was obtained for many samples as shown in Fig. 4c and 4d. To determine θ that was defined as the angle between the tangent to a given edge and AC directions ($0 < \theta < 120^\circ$) that are represented with the double-headed arrows within the AFM images. Between the two alternative ZZ directions, ZZ_M was assigned to the one that was parallel to the edges of TEs or TOs as explained earlier. Fig. 4c showed that k_θ of MoSe₂ reached maximum and minimum at $\theta = 90$ and 30° , representing k_{ZZX} and k_{ZZM} , respectively, and intermediate values for 60° that corresponded to k_{AC} . Whereas k_θ of WSe₂ exhibited a similar pattern (Fig. 4d), its modulation among different edges was significantly reduced (maximum/minimum = 1.5).

These results that directly mapped anisotropic reactions agreed with observed triangular patterns of varying anisotropy index. Specifically, the triangles of MoSe₂ with small anisotropy index values can be well represented by the case No. 4 of Fig. S6 ($k_{ZZX} : k_{AC} : k_{ZZM} = 1 : 0.77 : 0.55$). The increased isotropy in TOs of WSe₂ is consistent with the fact that the differences among the three k 's are less significant ($k_{ZZX} : k_{AC} : k_{ZZM} = 1 : 0.88 : 0.66$) than those of MoSe₂. In addition, the experimental edge-specific rates allowed us to validate whether the current reactions are consistent with the KWC model. For further quantification, k_θ of MoSe₂ and WSe₂ were fitted with a sinusoidal function with a constant background (Fig. 4c & 4d). Then, each fit could be represented by its minimum/maximum ratio (k_{ZZM}/k_{ZZX}), denoted R_E . In Fig. 4e, we simulated oxidation patterns that would grow from a point reaction center for a given set of k_θ (red line) represented by R_E . In the KWC limit, the edges of TEs and TOs will be shaped by the inner envelope of the Wulff lines in black. For the larger R_E , KWC

predicts the more rounded triangles. As shown in Fig. 4f, the anisotropy index (R) is essentially identical to R_E when $R_E > 0.7$. As R_E decreases to zero, the envelope approaches an equilateral triangle with the smallest R of 0.5. Notably, the experimental data in Fig. 4f suggest that MoSe₂ is consistent with the KWC prediction unlike WSe₂ which exhibited noticeable deviation.

Chemical nature of reaction centers. In Fig. 5a, we summarized the areal densities of TEs and TOs for the four TMDs. Because the distribution of the triangular objects varied significantly across samples (Fig. 1), the statistics showed sizable standard deviations as marked with the error bars. However, it is clear that metal selenides ($\sim 1 \times 10^9 \text{ cm}^{-2}$) exhibited an order of magnitude denser TEs or TOs than metal sulfides ($\sim 1 \times 10^8 \text{ cm}^{-2}$), which was valid irrespective of thickness. The robustness of sulfides is in line with their higher activation energy for dissociative adsorption of O₂ on chalcogen vacancies.⁴¹ In addition, the statistics on the number densities suggest that the underlying reaction mechanism is complex. In early studies on MoS₂,²¹⁻²² it was inferred that oxidation started at preexisting defects and proceeded synchronously based on the observation that the triangular patterns were similar in size. However, the observed areal densities of TEs and TOs were orders of magnitude lower than those for major structural defects found in the TMDs. Electron microscopy works^{14, 42-43} revealed that mono and di-vacancies of S are highly abundant ($10^{12} \sim 10^{13} \text{ cm}^{-2}$) and indicates that vacancies of a few atoms and antisites were also more frequent than TEs and TOs. In a control experiment, we tested high-quality WSe₂ samples, grown in the self-flux method, that have 100 times fewer point defects than the conventional crystals grown by chemical vapor transport (CVT).²⁶ However, their TO density was not meaningfully different from that of the samples exfoliated from CVT-grown crystals (Fig. S7). This indicates that the most abundant single-atom defects that were greatly reduced in the flux-grown WSe₂ are insufficient to serve alone as the reaction centers. As shown in Fig. 5b, no TOs were found in 2L WSe₂ samples supported on hBN substrates except at the hBN steps of 12 nm in height, which induce significant lattice strain in TMDs (Fig. S8). The density was estimated to be at least two orders of magnitude smaller on flat hBN than on SiO₂/Si substrates (Fig. S7). These results led us to conclude

that the observed TEs and TOs are initiated at lattice sites that are deformed by the interaction with underlying substrates.

This interpretation is consistent with the fact that the edges of WSe₂ underwent oxidation even when supported on hBN (Fig. S8c). We also note that TEs and TOs had fairly broad size distributions (Fig. S9), which result from unknown heterogeneity in the nucleation or propagation steps of the reaction. Otherwise, one would obtain a very narrow distribution as seen in the oxidation of graphite¹² or multilayer graphene.² 2D materials conform to the underlying substrates⁴⁴⁻⁴⁵ because of substantial adhesion energy,⁴⁶ which leads to atomic-scale corrugation in their structure.⁴⁷ Widely varying reactivity in the oxidation of graphene was attributed to such substrate-mediated deformation.² It is likely that the lattice sites serving as reaction centers are further deformed in-situ through a thermally activated process at elevated temperatures.⁴ This is also consistent with the 10-fold larger density of TO_B than TO_T (Fig. 2e), as the bottommost layers in contact with the substrates are more susceptible to chemical perturbation. Besides the lattice sites deformed by substrates, the reaction may be initiated by diffusional coalescence of point defects.⁴⁸ At elevated temperatures, S vacancies were observed to diffuse efficiently and merge into line defects⁴⁹ or nanopores,⁵⁰ and transition metal atoms could also be exchanged.⁵¹ Mechanistic understanding of the initiation step requires further experimental and theoretical studies.

Conclusions

In summary, we reported material-dependent anisotropy in the thermal oxidation of four 2D TMDs that led to randomly distributed arrays of aligned triangular patterns. SHG spectroscopy combined with AFM method allowed us to quantify the reaction rates as a function of crystallographic direction. For all of the TMDs, the reactions proceeded fastest (slowest) at chalcogen-terminated (metal-terminated) ZZ edges with AC edges in the middle. The degree of anisotropy related to the roundness of the triangles was higher for W dichalcogenides than Mo counterparts and exhibited opposite dependence on

thickness. The overall trigonal shapes agreed with the simulations by kinetic Wulff construction based on the experimental edge-specific rates but with noticeable deviation for W diselenides. We also show that the reactions are initiated at substrate-mediated defects that are located on the bottom and top surfaces of 2D TMDs.

Methods

Preparation and Treatments of Samples. 2D samples of four TMDs (MoS₂, MoSe₂, WS₂, and WSe₂) and hBN were prepared by mechanically exfoliating²⁵ their bulk crystals (natural MoS₂; CVT-grown MoSe₂, WS₂, and WSe₂ from 2D Semiconductors Inc.). Some WSe₂ samples were exfoliated from high-quality bulk crystals grown by a self-flux method.²⁶ Si substrates with 285 nm SiO₂ were treated with UV-generated ozone before the mechanical exfoliation. WSe₂ supported on multilayer hBN was fabricated by dry transfer method. Thermal oxidation was carried out in a mixed gas flow of O₂ (0.05 L/min) and Ar (0.20 L/min) using a quartz-tube furnace (Lindberg, Blue M) as described in a previous paper.²⁰ The temperature of the reactor was chosen in the range of 280 ~ 380 °C, and the reaction was continued for 2 h unless noted otherwise.

Raman and photoluminescence spectroscopy. The thickness and quality of each TMD sample were identified with differential reflectance²⁷ and Raman spectroscopy.²⁸ Raman and PL spectra were obtained with a home-built micro-Raman spectrometer setup described elsewhere.²⁹ Briefly, a laser beam operated at 457 nm was focused onto a sample with a spot size of ~1 μm using a microscope objective (40×, numerical aperture = 0.60). Backscattered signals were collected with the same objective and guided to a spectrometer equipped with a liquid nitrogen-cooled CCD detector. The overall spectral accuracy of Raman and PL measurement was better than 1 and 5 cm⁻¹, respectively. The average power on the sample surface was maintained below 0.2 mW to avoid photoinduced effects.

AFM measurements. The topological details of samples were investigated using an atomic force microscope (Park Systems, XE-70) before and after thermal oxidation. Height and phase images were

obtained in a noncontact mode unless noted otherwise, whereas LFM images were obtained in a contact mode. The nominal radius of Si tips was 8 nm (MicroMasch, NSC-15 for noncontact and CSC-17 for contact mode).

SHG spectroscopy. SHG measurements were performed with a home-built setup configured upon a commercial microscope (Nikon, Ti-U) as described elsewhere.²⁰ Briefly, the plane-polarized output from a Ti:sapphire laser (Coherent Inc., Chameleon) was used as a fundamental pulse with duration and repetition rate of 140 fs and 80 MHz, respectively. The beam was focused on samples with a spot size of $\sim 2 \mu\text{m}$ using a microscope objective (40 \times , numerical aperture = 0.60). Backscattered SHG signals were collected with the same objective and guided to a spectrometer equipped with a thermoelectrically cooled CCD detector (Andor Inc., DU971P). An analyzing polarizer was placed in front of the spectrometer to select polarization components of interest. Samples were rotated with a precision of 0.2 degrees to vary the polarization angle of the incident fundamental beam.

ASSOCIATED CONTENT

Supporting Information. AFM height and phase images of 1L TMDs, Raman and photoluminescence spectra of 3L WS₂, determination of crystallographic orientation, complementary AFM images of four multilayer TMDs, TEs in multilayer MoSe₂, oxidation patterns predicted by the KWC theory, density of reaction centers, no reactions for WSe₂ supported on hBN, size distribution of TOs in 1L WSe₂. This material is available free of charge via the Internet at <http://pubs.acs.org>.

AUTHOR INFORMATION

Corresponding Author

*E-mail: sunryu@postech.ac.kr

Author Contributions

The manuscript was written through the contributions of all authors. All authors have given approval to the final version of the manuscript.

Notes

The authors declare no conflict of interest.

ACKNOWLEDGMENTS

This work was supported by the National Research Foundation of Korea (NRF-2020R1A2C2004865 and NRF- 2019R1A4A1027934).

REFERENCES

- (1) Rothenberg, G., *Catalysis: concepts and green applications*. 2nd ed.; Wiley-VCH: 2017.
- (2) Liu, L.; Ryu, S.; Tomasik, M. R.; Stolyarova, E.; Jung, N.; Hybertsen, M. S.; Steigerwald, M. L.; Brus, L. E.; Flynn, G. W., Graphene oxidation: thickness dependent etching and strong chemical doping. *Nano Lett.* **2008**, 8, 1965-1970.
- (3) Schedin, F.; Geim, A. K.; Morozov, S. V.; Hill, E. W.; Blake, P.; Katsnelson, M. I.; Novoselov, K. S., Detection of individual gas molecules adsorbed on graphene. *Nat. Mater.* **2007**, 6 (9), 652-655.
- (4) Ryu, S.; Liu, L.; Berciaud, S.; Yu, Y.-J.; Liu, H.; Kim, P.; Flynn, G. W.; Brus, L. E., Atmospheric oxygen binding and hole doping in deformed graphene on a SiO₂ substrate. *Nano Lett.* **2010**, 10 (12), 4944-4951.
- (5) Lee, D.; Ahn, G.; Ryu, S., Two-dimensional water diffusion at a graphene-silica interface. *J. Am. Chem. Soc.* **2014**, 136 (18), 6634-6642.
- (6) Park, K.; Kang, H.; Koo, S.; Lee, D.; Ryu, S., Redox-governed charge doping dictated by interfacial diffusion in two-dimensional materials. *Nat. Commun.* **2019**, 10 (1), 4931.
- (7) Ohta, T.; Bostwick, A.; Seyller, T.; Horn, K.; Rotenberg, E., Controlling the electronic structure of bilayer graphene. *Science* **2006**, 313 (5789), 951-954.
- (8) Chen, Z. Y.; Berciaud, S.; Nuckolls, C.; Heinz, T. F.; Brus, L. E., Energy transfer from individual semiconductor nanocrystals to graphene. *ACS Nano* **2010**, 4 (5), 2964-2968.

(9) Xie, L.; Ling, X.; Fang, Y.; Zhang, J.; Liu, Z., Graphene as a substrate to Suppress fluorescence in resonance Raman spectroscopy. *J. Am. Chem. Soc.* **2009**, *131* (29), 9890-9891.

(10) Swathi, R. S.; Sebastian, K. L., Resonance energy transfer from a dye molecule to graphene. *The Journal of Chemical Physics* **2008**, *129* (5), 054703.

(11) Raja, A.; Montoya-Castillo, A.; Zultak, J.; Zhang, X.-X.; Ye, Z.; Roquelet, C.; Chenet, D. A.; van der Zande, A. M.; Huang, P.; Jockusch, S.; Hone, J.; Reichman, D. R.; Brus, L. E.; Heinz, T. F., Energy transfer from quantum dots to graphene and MoS₂: the role of absorption and screening in two-dimensional materials. *Nano Lett.* **2016**, *16* (4), 2328-2333.

(12) Lee, S. M.; Lee, Y. H.; Hwang, Y. G.; Hahn, J. R.; Kang, H., Defect-induced oxidation of graphite. *Phys. Rev. Lett.* **1999**, *82* (1), 217-220.

(13) Jaramillo, T. F.; Jørgensen, K. P.; Bonde, J.; Nielsen, J. H.; Horch, S.; Chorkendorff, I., Identification of active edge sites for electrochemical H₂ evolution from MoS₂ nanocatalysts. *Science* **2007**, *317* (5834), 100-102.

(14) Qiu, H.; Xu, T.; Wang, Z.; Ren, W.; Nan, H.; Ni, Z.; Chen, Q.; Yuan, S.; Miao, F.; Song, F.; Long, G.; Shi, Y.; Sun, L.; Wang, J.; Wang, X., Hopping transport through defect-induced localized states in molybdenum disulphide. *Nat. Commun.* **2013**, *4* (1), 2642.

(15) Bollinger, M. V.; Lauritsen, J. V.; Jacobsen, K. W.; Nørskov, J. K.; Helveg, S.; Besenbacher, F., One-dimensional metallic edge states in MoS₂. *Phys. Rev. Lett.* **2001**, *87* (19), 196803.

(16) Hu, Z.; Avila, J.; Wang, X.; Leong, J. F.; Zhang, Q.; Liu, Y.; Asensio, M. C.; Lu, J.; Carvalho, A.; Sow, C. H.; Castro Neto, A. H., The role of oxygen atoms on excitons at the edges of monolayer WS₂. *Nano Lett.* **2019**, *19* (7), 4641-4650.

(17) Yin, X.; Ye, Z.; Chenet, D. A.; Ye, Y.; O'Brien, K.; Hone, J. C.; Zhang, X., Edge nonlinear optics on a MoS₂ atomic monolayer. *Science* **2014**, *344* (6183), 488-490.

(18) Shi, Z.; Yang, R.; Zhang, L.; Wang, Y.; Liu, D.; Shi, D.; Wang, E.; Zhang, G., Patterning graphene with zigzag edges by self-aligned anisotropic etching. *Adv. Mater.* **2011**, *23* (27), 3061-3065.

(19) Ma, T.; Ren, W.; Zhang, X.; Liu, Z.; Gao, Y.; Yin, L.-C.; Ma, X.-L.; Ding, F.; Cheng, H.-M., Edge-controlled growth and kinetics of single-crystal graphene domains by chemical vapor deposition. *Proceedings of the National Academy of Sciences* **2013**, *110* (51), 20386-20391.

(20) Ryu, Y.; Kim, W.; Koo, S.; Kang, H.; Watanabe, K.; Taniguchi, T.; Ryu, S., Interface-confined doubly anisotropic oxidation of two-dimensional MoS₂. *Nano Lett.* **2017**, *17* (12), 7267-7273.

(21) Zhou, H. Q.; Yu, F.; Liu, Y. Y.; Zou, X. L.; Cong, C. X.; Qiu, C. Y.; Yu, T.; Yan, Z.; Shen, X. N.; Sun, L. F.; Yakobson, B. I.; Tour, J. M., Thickness-dependent patterning of MoS₂ sheets with well-oriented triangular pits by heating in air. *Nano Research* **2013**, *6* (10), 703-711.

(22) Yamamoto, M.; Einstein, T. L.; Fuhrer, M. S.; Cullen, W. G., Anisotropic etching of atomically thin MoS₂. *J. Phys. Chem. C* **2013**, *117* (48), 25643-25649.

(23) Wang, S.; Rong, Y.; Fan, Y.; Pacios, M.; Bhaskaran, H.; He, K.; Warner, J. H., Shape evolution of monolayer MoS₂ crystals grown by chemical vapor deposition. *Chem. Mater.* **2014**, *26* (22), 6371-6379.

(24) Govind Rajan, A.; Warner, J. H.; Blankschtein, D.; Strano, M. S., Generalized mechanistic model for the chemical vapor deposition of 2D transition metal dichalcogenide monolayers. *ACS Nano* **2016**, *10* (4), 4330-4344.

(25) Novoselov, K. S.; Jiang, D.; Schedin, F.; Booth, T. J.; Khotkevich, V. V.; Morozov, S. V.; Geim, A. K., Two-dimensional atomic crystals. *Proc. Natl. Acad. Sci. U. S. A.* **2005**, *102* (30), 10451-10453.

(26) Edelberg, D.; Rhodes, D.; Kerelsky, A.; Kim, B.; Wang, J.; Zangiabadi, A.; Kim, C.; Abhinandan, A.; Ardelean, J.; Scully, M.; Scullion, D.; Embon, L.; Zu, R.; Santos, E. J. G.; Balicas, L.; Marianetti, C.; Barmak, K.; Zhu, X.; Hone, J.; Pasupathy, A. N., Approaching the intrinsic limit in transition metal diselenides via point defect control. *Nano Lett.* **2019**, *19* (7), 4371-4379.

(27) Lee, J.; Ko, T. Y.; Kim, J. H.; Bark, H.; Kang, B.; Jung, S. G.; Park, T.; Lee, Z.; Ryu, S.; Lee, C., Structural and optical properties of single-and few-layer magnetic semiconductor CrPS₄. *ACS Nano* **2017**, *11* (11), 10935-10944.

(28) Lee, C.; Yan, H.; Brus, L. E.; Heinz, T. F.; Hone, J.; Ryu, S., Anomalous lattice vibrations of single- and few-Layer MoS₂. *ACS Nano* **2010**, *4* (5), 2695-2700.

(29) Lee, J. E.; Ahn, G.; Shim, J.; Lee, Y. S.; Ryu, S., Optical separation of mechanical strain from charge doping in graphene. *Nat. Commun.* **2012**, *3*, 1024.

(30) Almonte, L.; Colchero, J., True non-contact atomic force microscopy imaging of heterogeneous biological samples in liquids: topography and material contrast. *Nanoscale* **2017**, *9* (8), 2903-2915.

(31) Feldman, Y.; Wasserman, E.; Srolovitz, D. J.; Tenne, R., High-rate, gas-phase growth of MoS₂ nested inorganic fullerenes and nanotubes. *Science* **1995**, *267*, 222.

(32) *CRC Handbook of Chemistry and Physics*. Internet Version 2005 ed.; CRC Press: Boca Raton, 2005

(33) Li, Y.; Rao, Y.; Mak, K. F.; You, Y.; Wang, S.; Dean, C. R.; Heinz, T. F., Probing symmetry properties of few-layer MoS₂ and h-BN by optical second-harmonic generation. *Nano Lett.* **2013**, *13* (7), 3329-3333.

(34) Lv, D.; Wang, H.; Zhu, D.; Lin, J.; Yin, G.; Lin, F.; Zhang, Z.; Jin, C., Atomic process of oxidative etching in monolayer molybdenum disulfide. *Science Bulletin* **2017**, *62* (12), 846-851.

(35) Li, J.; Hu, S.; Chen, Z.; Liang, Y.; Kang, H.; Zhang, Y.; Sui, Y.; Wang, S.; Yu, G.; Peng, S.; Jin, Z.; Liu, X., Facile and rigorous route to distinguish the boundary structure of monolayer MoS₂ domains by oxygen etching. *Appl. Surf. Sci.* **2020**, *510*, 145412.

(36) Lee, C.; Li, Q. Y.; Kalb, W.; Liu, X. Z.; Berger, H.; Carpick, R. W.; Hone, J., Frictional characteristics of atomically thin sheets. *Science* **2010**, *328* (5974), 76-80.

(37) Cao, D.; Shen, T.; Liang, P.; Chen, X.; Shu, H., Role of chemical potential in flake shape and edge properties of monolayer MoS₂. *The Journal of Physical Chemistry C* **2015**, *119* (8), 4294-4301.

(38) Ringe, E.; Van Duyne, R. P.; Marks, L. D., Kinetic and thermodynamic modified Wulff constructions for twinned nanoparticles. *The Journal of Physical Chemistry C* **2013**, *117* (31), 15859-15870.

(39) Einstein, T. L., Equilibrium shape of crystals. In *Handbook of Crystal Growth, Fundamentals*, 2nd ed.; Nishinaga, T., Ed. Elsevier: Amsterdam, 2015; Vol. 1A, pp 215-264.

(40) Ly, T. H.; Chiu, M.-H.; Li, M.-Y.; Zhao, J.; Perello, D. J.; Cichocka, M. O.; Oh, H. M.; Chae, S. H.; Jeong, H. Y.; Yao, F.; Li, L.-J.; Lee, Y. H., Observing grain boundaries in CVD-grown monolayer transition metal dichalcogenides. *ACS Nano* **2014**, *8* (11), 11401-11408.

(41) Liu, H.; Han, N.; Zhao, J., Atomistic insight into the oxidation of monolayer transition metal dichalcogenides: from structures to electronic properties. *RSC Adv.* **2015**, *5* (23), 17572-17581.

(42) Zhou, W.; Zou, X.; Najmaei, S.; Liu, Z.; Shi, Y.; Kong, J.; Lou, J.; Ajayan, P. M.; Yakobson, B. I.; Idrobo, J.-C., Intrinsic structural defects in monolayer molybdenum disulfide. *Nano Lett.* **2013**, *13* (6), 2615-2622.

(43) Hong, J. H.; Hu, Z. X.; Probert, M.; Li, K.; Lv, D. H.; Yang, X. N.; Gu, L.; Mao, N. N.; Feng, Q. L.; Xie, L. M.; Zhang, J.; Wu, D. Z.; Zhang, Z. Y.; Jin, C. H.; Ji, W.; Zhang, X. X.; Yuan, J.; Zhang, Z., Exploring atomic defects in molybdenum disulphide monolayers. *Nat. Commun.* **2015**, *6*, 6293.

(44) Stolyarova, E.; Rim, K. T.; Ryu, S.; Maultzsch, J.; Kim, P.; Brus, L. E.; Heinz, T. F.; Hybertsen, M. S.; Flynn, G. W., High-resolution scanning tunneling microscopy imaging of mesoscopic graphene sheets on an insulating surface. *Proc. Natl. Acad. Sci. U. S. A.* **2007**, *104* (22), 9209-9212.

(45) Cullen, W. G.; Yamamoto, M.; Burson, K. M.; Chen, J. H.; Jang, C.; Li, L.; Fuhrer, M. S.; Williams, E. D., High-fidelity conformation of graphene to SiO₂ topographic features. *Phys. Rev. Lett.* **2010**, *105* (21), 215504.

(46) Koenig, S. P.; Boddeti, N. G.; Dunn, M. L.; Bunch, J. S., Ultrastrong adhesion of graphene membranes. *Nat. Nanotechnol.* **2011**, *6* (9), 543-546.

(47) Geringer, V.; Liebmann, M.; Echtermeyer, T.; Runte, S.; Schmidt, M.; Rućkamp, R.; Lemme, M. C.; Morgenstern, M., Intrinsic and extrinsic corrugation of monolayer graphene deposited on SiO₂. *Phys. Rev. Lett.* **2008**, *102*, 076102.

(48) Trevethan, T.; Latham, C. D.; Heggie, M. I.; Briddon, P. R.; Rayson, M. J., Vacancy diffusion and coalescence in graphene directed by defect strain fields. *Nanoscale* **2014**, *6* (5), 2978-2986.

(49) Chen, Q.; Li, H.; Zhou, S.; Xu, W.; Chen, J.; Sawada, H.; Allen, C. S.; Kirkland, A. I.; Grossman, J. C.; Warner, J. H., Ultralong 1D vacancy channels for rapid atomic migration during 2D void formation in monolayer MoS₂. *ACS Nano* **2018**, *12* (8), 7721-7730.

(50) Ryu, G. H.; France-Lanord, A.; Wen, Y.; Zhou, S.; Grossman, J. C.; Warner, J. H., Atomic structure and dynamics of self-limiting sub-nanometer pores in monolayer WS₂. *ACS Nano* **2018**, *12* (11), 11638-11647.

(51) Bogaert, K.; Liu, S.; Chesin, J.; Titow, D.; Gradečak, S.; Garaj, S., Diffusion-mediated synthesis of MoS₂/WS₂ lateral heterostructures. *Nano Lett.* **2016**, *16* (8), 5129-5134.

FIGURES & CAPTIONS

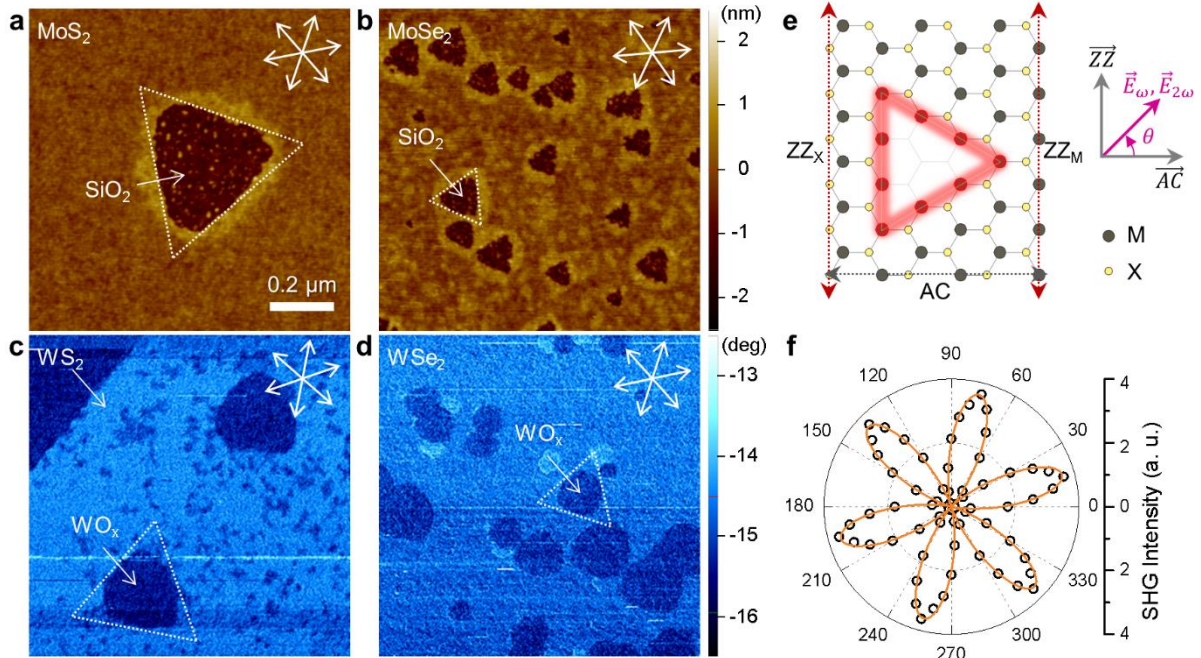


Figure 1. In-plane anisotropy in thermal oxidation of 1L TMDs. (a ~ b) AFM height images of triangular etch pits (TEs) of 1L MoS₂ (a) and MoSe₂ (b). (c ~ d) Phase images of triangular oxides (TOs) of 1L WS₂ (c) and WSe₂ (d). SHG-determined armchair directions are denoted by the double-headed arrows of 6-fold symmetry. Oxidation-generated triangular structures were shown with ZZ_M-edged triangles of white dotted lines. T_{ox} of (a ~ d) was 330, 290, 360, and 300 °C, respectively. (e) Scheme for polarized SHG measurements of 1L TMDs with ZZ_X (left edge), ZZ_M (right edge), AC edges (top and bottom), and ZZ_M-terminated TE (highlighted with a red triangle). The angle (θ) between AC edge and SHG signal ($\vec{E}_{2\omega}$), which was parallel to incident fundamental beam (\vec{E}_ω), was varied for the determination of crystallographic orientation. (f) SHG intensity of oxidized 1L WSe₂ given as a function of θ .

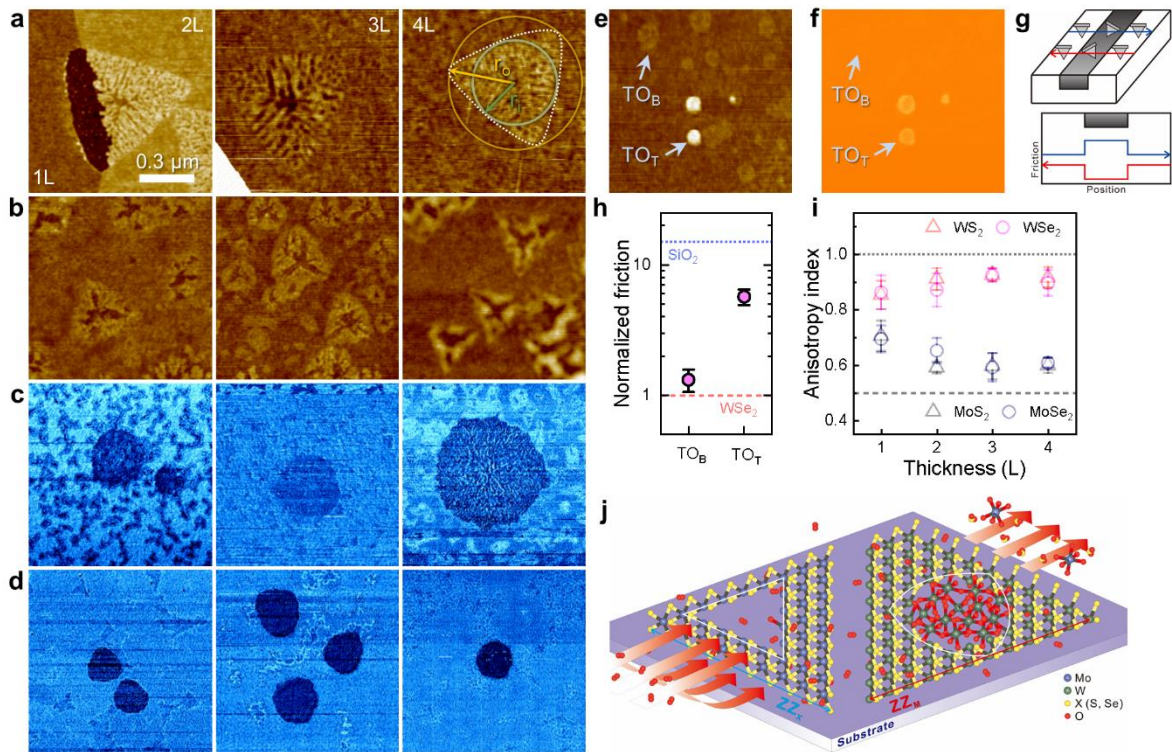


Figure 2. Diverse reactions in multilayer TMDs. (a ~ d) Height (a & b) and phase (c & d) images of oxidized MoS₂ (a), MoSe₂ (b), WS₂ (c), and WSe₂ (d): 2, 3, 4L in thickness from left to right. T_{ox} and t_{ox} are given in Fig. S4. All scale bars are 0.3 μ m. The anisotropy index (R) of the TO in 4L MoS₂ (a) was defined by r_i/r_0 , where r_i (r_0) is the radius of the circle that inscribes in (circumscribes on) the TO. (e & f) Height (e) and LFM (f) images of 2L WSe₂ ($T_{ox} = 300$ °C and $t_{ox} = 2$ h). (g) Scheme of LFM scans (top) and resulting frictional force profiles (bottom). (h) Frictional force of TOs in the top (TO_T) and bottommost (TO_B) layers of oxidized multilayer WSe₂. The red and blue lines represent pristine WSe₂ and SiO₂ substrates, respectively. (i) Anisotropy index of four TMDs as a function of thickness. (j) Reaction scheme for oxidation with differing anisotropy for Mo and W dichalcogenides: reactions may be initiated on the top and bottom surfaces of 1L and multilayers (1L is depicted for simplicity).

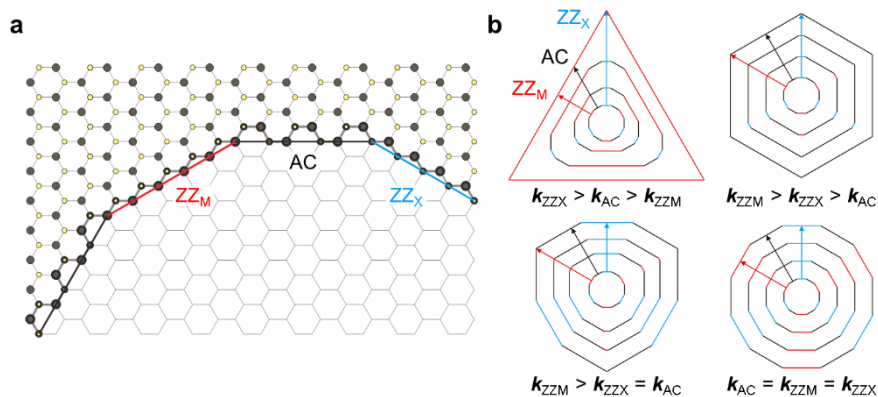


Figure 3. KWC-based prediction of oxidative etching patterns. (a) Schematic dodecagonal model as a reaction center with three representative edges: ZZ_M, AC, and ZZ_X represented by red, black, and blue lines, respectively. (b) Kinetic Wulff construction for four sets of (k_{ZZX} , k_{AC} , k_{ZZM}) that lead to triangles, hexagons, nonagons, and dodecagons, respectively. The innermost dodecagons are the reaction centers with the length of each arrow representing the rate (k) of each edge. (see Fig. S6 for all possible combinations)

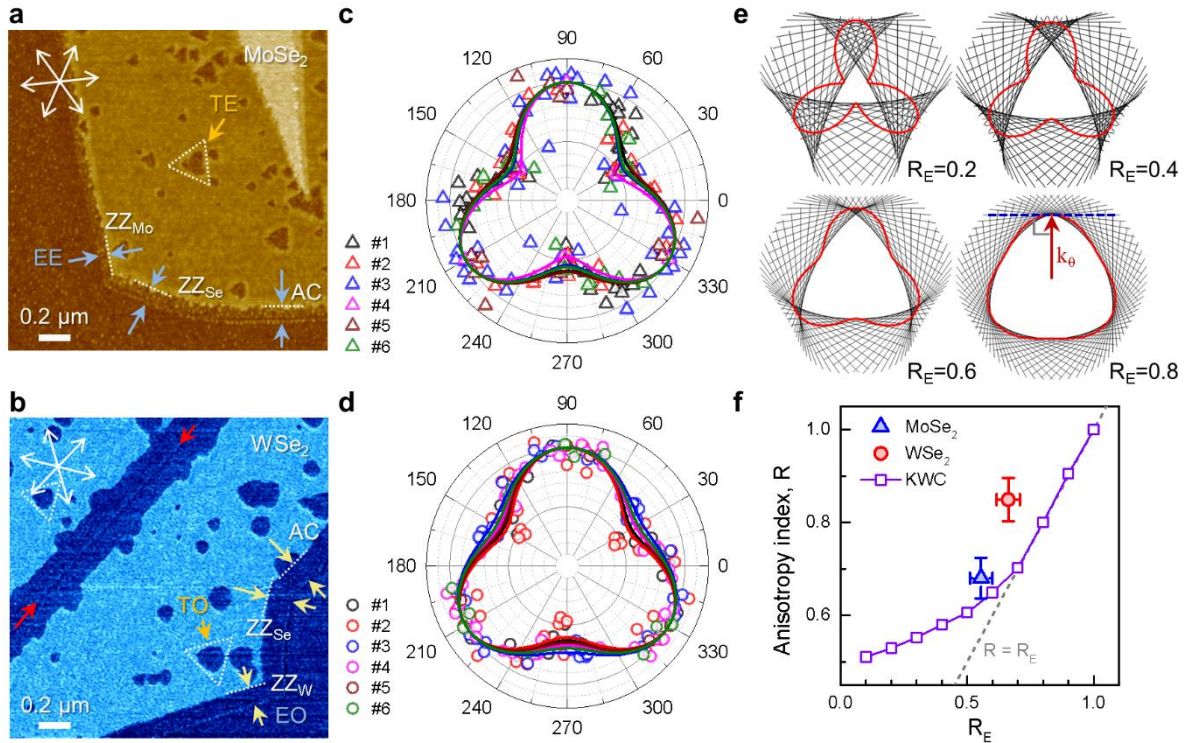


Figure 4. Determination of edge-specific rates and kinetic Wulff construction. (a ~ b) Height (a) and phase (b) images of oxidized 1L MoSe₂ ($T_{\text{ox}} = 290 \text{ }^{\circ}\text{C}$, $t_{\text{ox}} = 2 \text{ h}$) and 1L WSe₂ ($T_{\text{ox}} = 300 \text{ }^{\circ}\text{C}$, $t_{\text{ox}} = 2 \text{ h}$), respectively. In addition to TEs and TOs, the outer edges of MoSe₂ and WSe₂ underwent edge etching (EE) and edge oxidation (EO), respectively. The degree of edge reaction was marked by a pair of blue or yellow arrows. The differentiation between ZZ_M and ZZ_{Se} was made with respect to the orientation of TEs or TOs (see the main text). (c ~ d) Normalized reaction rate for EE of MoSe₂ (c) and EO of WSe₂ (d) obtained as a function of edge direction: 0, 30, and 90° respectively correspond to AC, ZZ_M, and ZZ_X as defined in Fig. 1e. Because of the 3-fold symmetry of the lattice, data sets determined for 0 ~ 120° were repeated every 120° and fitted with a sinusoidal function (see Supplementary Note). (e) 2D KWC of oxidative etching simulated for the experimental edge-dependent reaction rates (red curve), where R_E is the ratio of minimum to maximum rates for edge reactions. The kinetic Wulff shape is given as the interior envelope formed by the Wulff lines (in black), one of which in blue ($R_E = 0.8$) is

shown to be normal to k_θ . (f) Relation between the anisotropy index R and R_E obtained from (e). The experimental data for MoSe_2 and WSe_2 are given with the line for $R = R_E$.

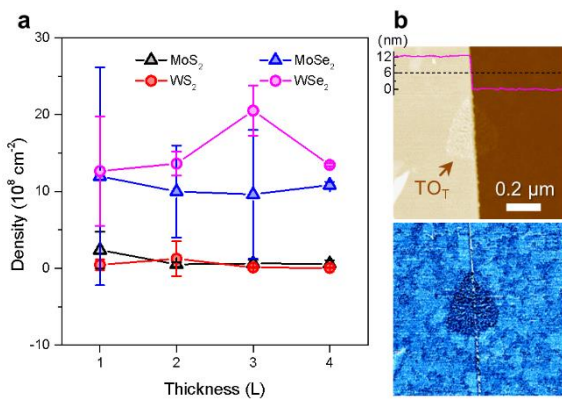


Figure 5. Density and origin of reaction centers. (a) Density of TEs and TOs for four TMDs of $1 \sim 4\text{L}$. (b) Height (top) and phase (bottom) images of 2L WSe_2 supported on hBN. TOs were found only at the hBN step of $\sim 12 \text{ nm}$ in height as shown by the height profile in magenta.

TOC Figure

